AGU PUBLICATIONS

JGR

Journal of Geophysical Research: Solid Earth

RESEARCH ARTICLE
10.1002/2014JB011221

Key Points:
- In situ sonic logs match well with the ultrasonic laboratory measurements
- Tectonic load by thrusting overprinted the primary petrophysical properties
- Porosity changes are useful for quantitative paleostress reconstruction

Supporting Information:
- Readme
- Figure S1
- Figure S2

Correspondence to:
F. Trippetta,
fabio.trippetta@uniroma1.it

Citation:
Smeraglia, L., F. Trippetta, E. Carminati, and S. Mollo (2014), Tectonic control on the petrophysical properties of foredeep sandstone in the Central Apennines, Italy, *J. Geophys. Res. Solid Earth*, *119*, 9077–9094, doi:10.1002/2014JB011221.

Received 23 APR 2014
Accepted 30 OCT 2014
Accepted article online 5 NOV 2014
Published online 3 DEC 2014

Tectonic control on the petrophysical properties of foredeep sandstone in the Central Apennines, Italy

Luca Smeraglia[1], Fabio Trippetta[1], Eugenio Carminati[1,2], and Silvio Mollo[3]

[1]Dipartimento di Scienze della Terra, Sapienza Universita' di Roma, Rome, Italy, [2]Istituto di Geologia Ambientale e Geoingegneria, CNR, Rome, Italy, [3]Istituto Nazionale di Geofisica e Vulcanologia, Rome, Italy

Abstract Petrophysical properties of rocks and their applicability at larger scale are a challenging topic in Earth sciences. Petrophysical properties of rocks are severely affected by boundary conditions, rock fabric/microstructure, and tectonics that require a multiscale approach to be properly defined. Here we (1) report laboratory measurements of density, porosity, permeability, and *P* wave velocities at increasing confining pressure conducted on Miocene foredeep sandstones (Frosinone Formation); (2) compare the laboratory results with larger-scale geophysical investigations; and (3) discuss the effect of thrusting on the properties of sandstones. At ambient pressure, laboratory porosity varied from 2.2% to 13.8% and *P* wave velocities (V_p) from 1.5 km/s to 2.7 km/s. The *P* wave velocity increased with confining pressure, reaching between 3.3 km/s and 4.7 km/s at 100 MPa. In situ V_p profiles, measured using sonic logs, matched the ultrasonic laboratory measurement well. The permeability varied between 1.4×10^{-15} m^2 and 3.9×10^{-15} m^2 and was positively correlated with porosity. The porosity and permeability of samples taken at various distances to the Olevano–Antrodoco fault plane progressively decreased with distance while *P* wave velocity increased. At about 1 km from the fault plane, the relative variations reached 43%, 65%, and 20% for porosity, permeability, and *P* wave velocity, respectively. This suggests that tectonic loading changed the petrophysical properties inherited from sedimentation and diagenesis. Using field constraints and assuming overburden-related inelastic compaction in the proximity of the fault plane, we conclude that the fault reached the mechanical condition for rupture in compression at differential stress of 64.8 MPa at a depth of 1500 m.

1. Introduction

The knowledge of the petrophysical properties of rocks is crucial in many fields, such as the relocalization of earthquakes using appropriate velocity profiles [e.g., *Bally et al*., 1986; *Barchi et al*., 1998] and the characterization of water and hydrocarbon reservoirs [e.g., *Cosentino et al*., 2010]. Many works demonstrated that petrophysical properties of rocks are severely affected by boundary conditions [e.g., *Heap et al*., 2014a], rock fabric [e.g., *Benson et al*., 2005; *Heap et al*., 2014b], and by tectonic structures, such as faults [e.g., *Faulkner et al*., 2006; *Mitchell and Faulkner*, 2012]. Several studies were dedicated to local-scale changes of petrophysical properties and rock textures associated with fault development [*Chester and Logan*, 1986; *Tondi et al*., 2006; *Agosta et al*., 2007; *Solum et al*., 2010; *Mitchell and Faulkner*, 2012, and references therein], in particular for granular host rocks such as sandstones [*Antonellini and Aydin*, 1994, 1995; *Shipton and Cowie*, 2001; *Shipton et al*., 2002]. However, studies dedicated to the kilometer-scale variation of their petrophysical properties with respect to tectonic structures are rather scarce [e.g., *Benson et al*., 2005; *Chang et al*., 2006; *Mavko et al*., 2009]. Concerning the Central Apennines, a Tertiary-Present fold-and-thrust belt characterized by the occurrence of several carbonate ridges thrusted onto siliciclastic foredeep deposits [*Cosentino et al*., 2010], studies dedicated to the experimental evaluation of the petrophysical properties mainly focused on evaporites [*Trippetta et al*., 2010, 2013], carbonates [*Ciccotti and Mulargia*, 2004; *Ciccotti et al*., 2004], and fault rocks [*Agosta et al*., 2007]. It is worth noting that foredeep sandstones are common in mountain belts and represent the most common reservoir rocks worldwide. In this work, we report for the first time in the Apennines a set of laboratory measurements of petrophysical parameters (porosity, permeability, and seismic wave velocity) in siliciclastic sandstones belonging to the Tortonian Frosinone Formation that crop out at the footwall of the Olevano–Antrodoco thrust fault (Figure 1). Measurements were conducted at ambient temperature and pressure and at increasing confining pressure, simulating progressively deeper crustal

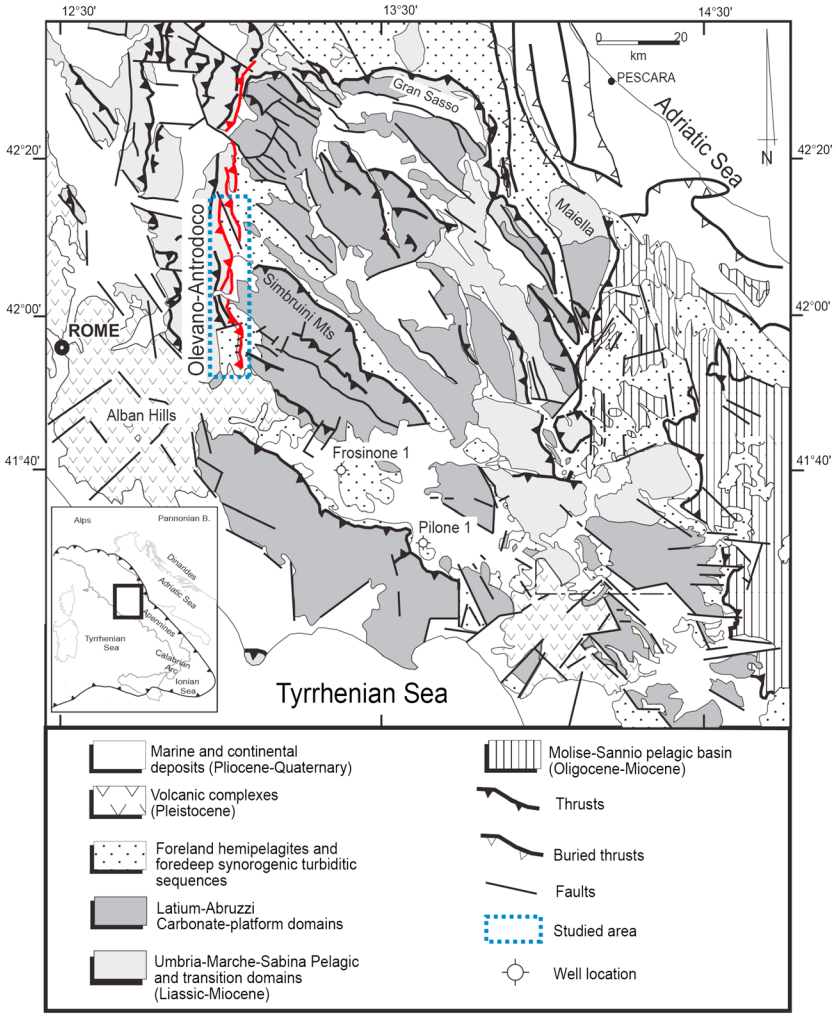

Figure 1. Schematic map of Central Apennines showing the studied area and the well locations. Modified from *Cavinato and De Celles* [1999].

conditions. The results were consistent with data from borehole sonic logs. Moreover, we attributed the observed variations of the petrophysical properties to the tectonic load associated with the Olevano–Antrodoco thrust fault.

The measurement of crustal stress magnitude is always challenging and generally poorly constrained [*Montone et al.*, 2012]. Moreover, in situ measurements in boreholes drilled for this purpose are extremely expensive [e.g., *Chéry et al.*, 2004; *Hickman and Zoback*, 2004; *Wu et al.*, 2007; *Tembe et al.*, 2009]. This is particularly significant in active fault zones where the knowledge of stress magnitude is crucial for understanding fault mechanics during earthquakes nucleation. Indirect stress evaluations on exhumed faults, as the Olevano–Antrodoco thrust, can be an inexpensive but valuable alternative. In this work we propose a workflow using laboratory values of porosity as a proxy for quantitative paleostress reconstruction. The procedure can be applied to other cases in fold-and-thrust belts worldwide.

2. Geological Setting

The Apennines are a late Oligocene-Present fold-and-thrust belt that developed along the "eastward" radially retreating subduction of the Adriatic Plate [e.g., *Carminati et al.*, 2012]. The Central Apennines (Figure 1) are characterized by the northeastward migration of thrust fronts [*Cipollari et al.*, 1995] that brought carbonate ridges onto foredeep turbiditic basins [*Ricci Lucchi*, 1986; *Boccaletti et al.*, 1990; *Cipollari et al.*, 1995; *Patacca and Scandone*, 2001; *Cosentino et al.*, 2010].

The rocks cropping out in the central sector of the Apennines fold-and-thrust belt were mainly deposited in two paleogeographic domains: the Latium–Abruzzi domain to the east and the Umbria–Marche domain to the west, both developed along the passive margin of the Adriatic Plate [*Carminati et al*., 2012]. The passive margin deposits consist of Late Triassic sulfates and dolomites [e.g., *Pierantoni et al*., 2005; *Ciarapica and Passeri*, 2005], followed by early Early Jurassic peritidal carbonate deposits [*Laubscher and Bernoulli*, 1977]. These deposits are common to both paleogeographic domains.

An Early Jurassic rifting phase generated structural highs and lows [*Santantonio and Carminati*, 2011]. To the west, the Umbria–Marche domain was characterized by deposition of Mesozoic–Tertiary limestones, marly limestones, and marls [*Centamore et al*., 1971; *Parotto and Praturlon*, 1975; *Corrado et al*., 1998] in a pelagic to escarpment environment, while shallow-water carbonate sedimentation continued until the Late Cretaceous in the Latium–Abruzzi domain (Figure 1) [*Damiani*, 1990, 1991].

In the Latium–Abruzzi domain, a Late Cretaceous-early Miocene hiatus was followed by deposition of early Miocene paraconformable carbonates, deposited along a carbonate ramp [*Civitelli and Brandano*, 2005] and hemipelagic marls deposited in a foreland environment [*Carminati et al*., 2007], followed by deposition of siliciclastic turbidites in a foredeep setting [*Patacca and Scandone*, 1989; *Cipollari and Cosentino*, 1991; *Patacca et al*., 1991; *Milli and Moscatelli*, 2000; *Critelli et al*., 2007]. *Corrado* [1994] showed that the siliciclastic deposits were buried at a maximum depth of about 2 km.

The siliciclastic turbidites are composed by fining upward meter-scale sequences consisting of fine- to medium-grained gray sandstones at the bottom, sometimes massive and amalgamated with frequent water-escape structures, passing upward to very fine grained laminated sandstones alternating with clay and marls with traction and fallout structures. The sandstones deposition likely occurred through poorly efficient turbiditic flows in elongated submarine-fan lobes, probably fed by deltas [*Milli and Moscatelli*, 2000]. Massive sandstones are the sedimentological expression of the lower and denser portion of bipartite turbidity currents, whereas laminated sandstones represent the upper, turbulent, and diluted portions [*Accordi et al*., 1986].

The shortening of the Central Apennine successions started in the late Miocene [*Bally et al*., 1986; *Mostardini and Merlini*, 1986; *Royden et al*., 1987]. The geometries and kinematics of Neogene contractional structures were strongly influenced by inherited Mesozoic faults and by the lateral variability in thickness and facies of sediments involved in the belt [e.g., *Calamita*, 1990; *Corrado et al*., 1998; *Butler and Mazzoli*, 2006]. The Olevano–Antrodoco thrust fault developed at the boundary between the Latium–Abruzzi platform and the Umbria–Marche basin, possibly inverting an Early Jurassic normal fault [*Di Domenica et al*., 2014].

2.1. The Olevano–Antrodoco Lineament

The Olevano–Antrodoco lineament is a N-S to NNE-SSW complex structure [*Dallan Nardi et al*., 1971; *Castellarin et al*., 1982], cropping out for tens of kilometers and separating the Umbria–Marche pelagic deposits to the west from the Latium–Abruzzi platform carbonates to the east (Figure 1). The thrust fault location was likely controlled by the occurrence of one or more Early Jurassic normal faults oriented N-S and dipping to the west [*Cantelli et al*., 1982].

The Olevano–Antrodoco is an out-of-sequence thrust fault [*Cipollari et al*., 1993] characterized by multiphase prevalently dextral transpressional kinematics [*Coli*, 1981; *Cavinato et al*., 1986; *Calamita and Deiana*, 1987; *Calamita et al*., 1987; *Corrado*, 1995; *Turtù et al*., 2013], although evidence for strike-slip kinematics on other fault segments oriented N-S in Central Apennines are reported by some authors [*Castellarin et al*., 1982; *Cello et al*., 1997; *Cello and Mazzoli*, 1999].

Our study focused on the southernmost 30 km of the lineament, where Miocene carbonates of the Calcari a Briozoi e Litotamni Formation [*Civitelli and Brandano*, 2005] and marly deposits of the Marne a Orbulina Formation [*Cipollari and Cosentino*, 1991] are thrusted onto the late Miocene siliciclastic foredeep sandstones of the Late Tortonian Frosinone Formation [*Cipollari and Cosentino*, 1991]. In its southernmost part, the Olevano–Antrodoco lineament displays an imbricate fan geometry (Figure 2). The number of splays, generally trending N-S and isolating thin slices of Miocene carbonates and marls, is variable from 5 to 1. The lateral continuity of the thrust fault is often interrupted by NW-SE and WNW-ESE subvertical transfer faults, displaying, respectively, dextral and sinistral strike-slip kinematics (Figure 2b).

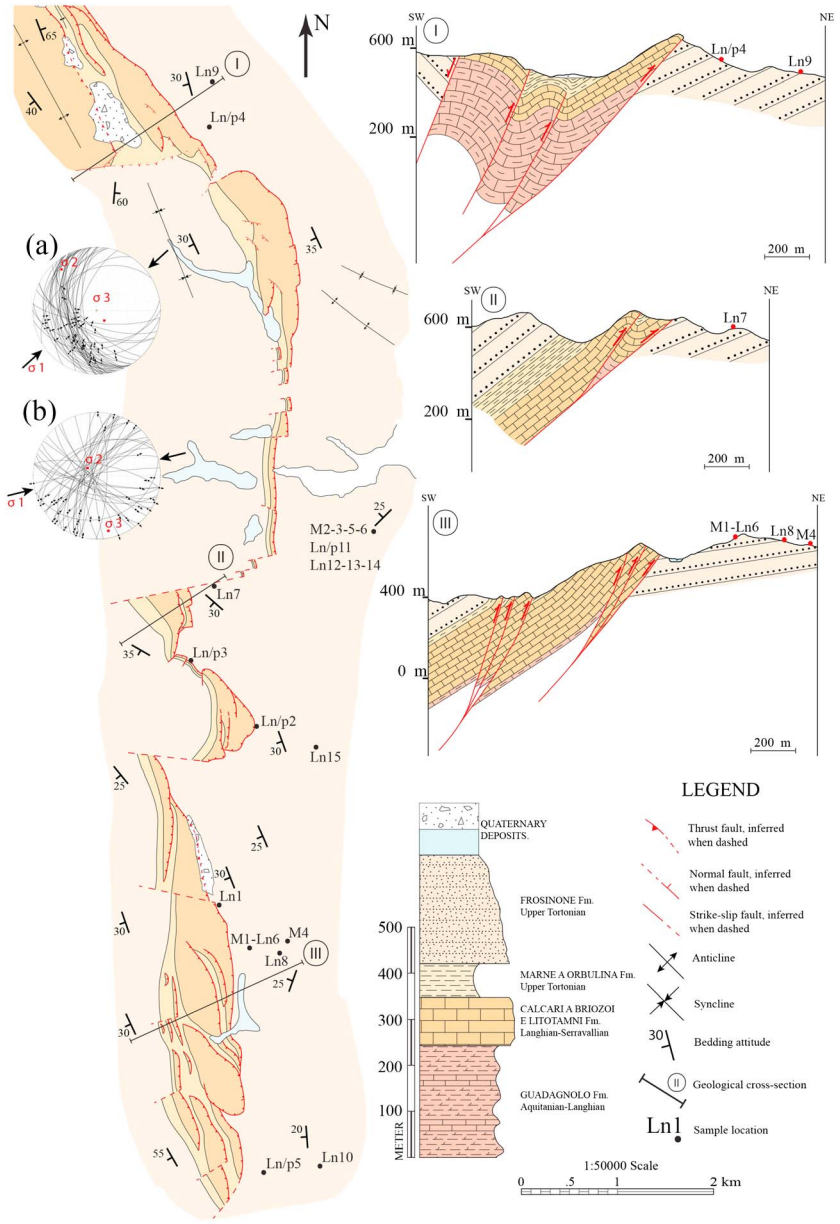

Figure 2. Schematic map of the southernmost sector of the Olevano–Antrodoco thrust fault with sampling localities. The geological cross sections show the stratigraphic and structural relationships between the Olevano–Antrodoco thrust and the Frosinone Formation. The stereoplots show (a) dextral transpressive and (b) right-lateral strike-slip faulting.

The hanging wall carbonates and marls are generally steeply dipping to the west, displaying hanging wall anticline geometries.

Detailed structural analysis allowed us to reconstruct the Olevano–Antrodoco kinematics. The main fault plane consists of gentle SW-dipping thrust plane with kinematic indicators showing mainly dextral transpression (Figure 2a). Data from kinematic indicators and slip vectors on fault planes exhibit top-to-NE slip directions, coherent with an axis of horizontal maximum compression oriented SW-NE.

At the footwall of the thrust fault, the turbiditic sequence gently dips toward W-WSW and NW (Figure 2), and no overturned footwall synclines were mapped (Figure 2). The footwall damage zone (in the sense of *Caine et al*. [1996]) is about 300 m wide and is associated with deformation bands, slip planes, fractures, and kilometer-scale open folds that fade moving eastward (i.e., away from the thrust surface).

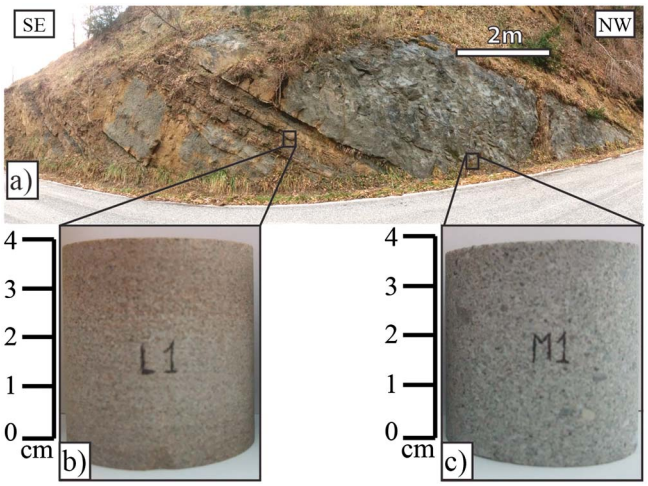

Figure 3. (a) Outcrop showing laminated and massive lithofacies of the Frosinone Formation. The outcrop is 15 m long and 1 km away from the thrust front. Cylindrical specimens of (b) laminated and (c) massive sandstones, displaying subhorizontal foliation and chaotic fabric, respectively.

3. Sampled Lithologies: Composition and Microstructural Observations

We analyzed 26 specimens of Miocene foredeep sandstones (Frosinone Formation) that were sampled at the footwall of the Olevano–Antrodoco thrust fault at various distances (Figure 2). For each sample, we calculated the stratigraphic distance from the thrust fault by measuring, perpendicularly to the bedding attitude, the distance between the sample location and the fault trace. Following *Milli and Moscatelli* [2000] and based on observed sedimentary features, the samples were classified as laminated (L) and massive (M) (Figure 3). Laminated samples are strongly anisotropic and consist of light yellow sandstone with low textural heterogeneity and clear planar bedding in both hand specimens and outcrops. A pervasive foliation is often visible in thin sections, where grains and clay minerals exhibit a preferred alignment that results in the lamination visible in hand specimens. Both intergranular and intragranular microcracks were recognized at the optical microscope scale; grains are generally angular to subrounded, very well sorted, with a mean size of approximately 0.2 mm (Figures 4a and 4b).

Massive samples are highly heterogeneous, and no lamination can be observed both in hand specimens and outcrops. Thin section investigation highlighted both intergranular and intragranular microcracks; grains appear poorly sorted, angular to subrounded, with variable sizes from 2 mm to $<$0.1 mm (Figures 4c and 4d). Largest grains are scattered in a matrix of smaller grains and do not show any preferred orientation. The largest (2 mm sized) grains are lithic fragments of metamorphic and sedimentary rocks or singles minerals (Figures 4c and 4d). According to *Chiocchini et al*. [1988], both lithofacies have a composition of about 33% quartz, 15% feldspar (plagioclase and K-feldspar), 5% lithics fragments (volcanic, metamorphic, and sedimentary rocks), and 20% mica together with other accessory minerals. The sandstones are cemented by calcite overgrowths that partially obliterated the primary porosity. According to *Cipollari et al*. [1993], the Olevano–Antrodoco thrust acted as an out-of-sequence thrust after the deposition of the Frosinone Formation sandstones, whose diagenesis and deposition were not affected by thrusting. Moreover, cements are homogeneously distributed throughout the stratigraphic levels of Frosinone Formation [*Chiocchini et al*., 1988], suggesting that with the exception of burial pressure, the boundary conditions during diagenesis were similar for the entire formation.

Laminated sandstones, close to the fault plane up to a distance of about 300 m, are often characterized by bands of crushed and comminuted minerals, showing a smaller grain size with respect to the host rock. These bands sometimes accommodate shear offset (Figure 4e) and are arranged as individual structures (up to 2 mm thick) or clusters (up to 1 cm thick). Cluster structures are made up of many adjacent bands forming ≈1 cm thick deformation zones. At the mesoscale, these structures are lighter in color and are characterized by differential erosion, compared to the host rock. We interpreted these bands as deformation bands [*Aydin*, 1978], e.g., as the result of strain localization processes [*Baud et al*., 2000; *Baud et al*., 2004; *Solum et al*., 2010; *Wong and Baud*, 2012]. Deformation bands are found in a wide range of geological settings [*Fossen et al*., 2007] and are often associated with damage zones in granular fault rocks [e.g., *Antonellini and Aydin*, 1994, 1995; *Solum et al*., 2010; *Ballas et al*., 2014]. They are characterized by a marked decrease in porosity and permeability [*Zhu and Wong*, 1997; *Wong and Baud*, 2012]. In the Frosinone Formation, deformation bands were found only in laminated sandstones (characterized by well-sorted grain size) close to the fault plane, consistently with the observations of *Cheung et al*. [2012].

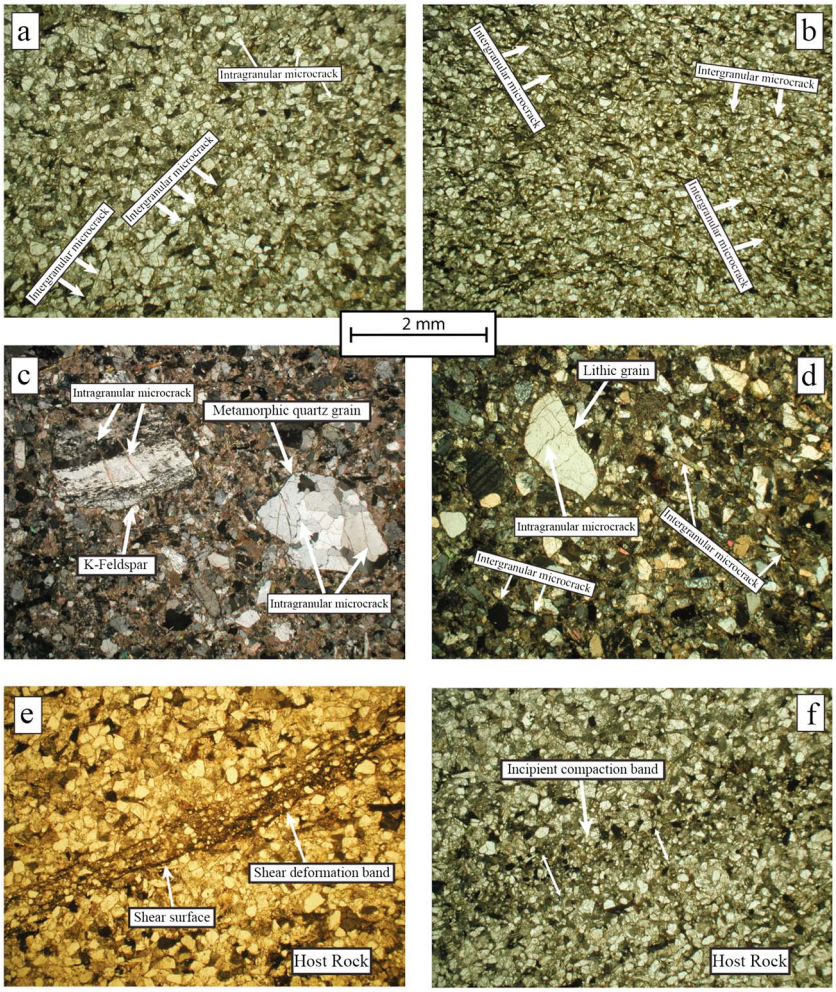

Figure 4. Thin sections representative of microstructures in the tested materials. (a and b, plane-polarized light) Laminated sandstones (Ln10 and Ln14) show low textural heterogeneities with preferentially aligned grains reproducing the same foliation of hand specimens. Both intergranular and intragranular microcracks are present, and minerals are generally angular to subrounded, very well sorted, and have a mean size of approximately 0.2 mm. (c and d, cross-polarized light) Massive sandstones (M1 and M4) show high textural heterogeneity, without clear foliation or fabric. Both intergranular and intragranular microcracks are present, and grains are poorly sorted, angular to subrounded, with variable sizes (from 2 mm to $<$0.1 mm), arranged randomly without any internal organization. The largest (2 mm) grains are lithic fragments of metamorphic and sedimentary rocks or single minerals. (e, plane-polarized light) Example of shear deformation band developed within fault damage zone. (f, plane-polarized light) Sample Ln2 shows an individual, 1 mm thick, band of crushed, and comminuted minerals, interpreted as an incipient compaction band.

Given the purpose of defining a general trend of petrophysical properties for the Frosinone Formation, we did not sample sandstones with deformation bands. Only in sample Ln2, an incipient compaction band, without any evidence of shear, was observed at the microscale (Figure 4f).

4. Methods

A set of 26 rock specimens was prepared and measured at the HP-HT Laboratory of Experimental Volcanology and Geophysics of the Istituto Nazionale di Geofisica e Vulcanologia (INGV) in Rome, Italy. Density, porosity, *P* wave velocity, and permeability measurements were conducted on cylindrical specimens 38 mm in diameter and 40 mm in length, with their end faces ground flat and parallel to better than ±0.02 mm. In order to avoid the effects of atmospheric weathering, we cored the specimens away from weathered surfaces. For laminated sandstones, measurements were performed on rock samples cored both normal (Ln) and

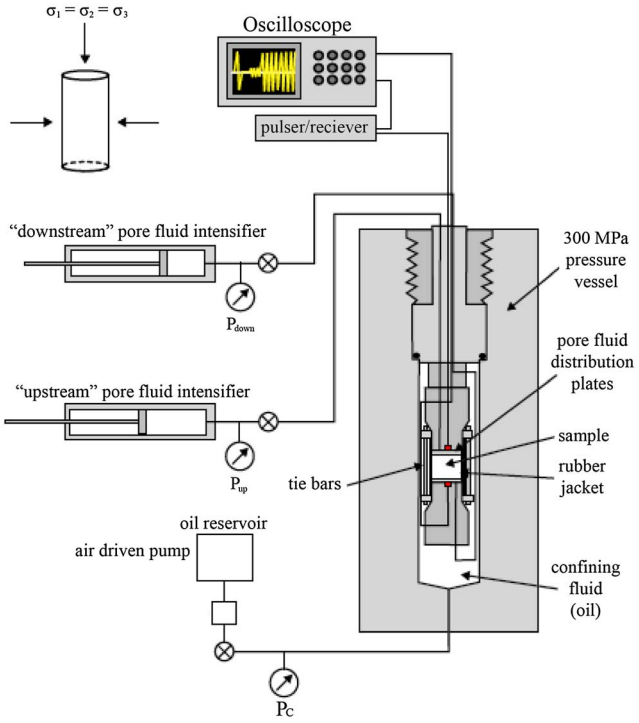

Figure 5. Schematic diagram of permeameter/volumometer at the HP-HT Laboratory of Experimental Volcanology and Geophysics of the Istituto Nazionale di Geofisica e Vulcanologia (INGV) in Rome, Italy, used for simultaneous porosity, permeability, and acoustic wave velocity measurements [from *Heap et al.*, 2014a].

parallel (Lp) to the observed foliation. On massive sandstones, measurements were conducted with no specific directions, since foliations were absent in these rocks.

Density measurements were made on samples that were dried in an oven at 60°C for a minimum of 24 h. This modest temperature is used to preclude any possibility of thermal cracking in the samples prior the measurements [*Glover et al.*, 1995].

The volume of interconnected pores (the so-called effective porosity) was measured using a helium pycnometer (AccuPyc II 1340). For simplicity, we will refer to the effective porosity as "porosity" from here onward.

Initial elastic wave velocity measurements were performed axially on dry samples at ambient conditions using the pulse transmission technique [*Birch*, 1960, 1961]. A 900 V pulse generator was used to excite a 1 MHz resonant frequency piezoelectric transmitting transducer, and resulting waveforms were captured using an identical receiving transducer. After preamplification, signals were recorded and displayed on a digital storage oscilloscope.

Subsequently, axial *P* wave velocity measurements were performed at increasing pressure steps by means of a fluid-medium hydrostatic pressure vessel, equipped with four 1 MHz resonant frequency piezoelectric transducer crystals, two each for compressional (V_p) and shear (V_s) wave velocity measurements. Seismic velocities were measured under dry and wet (saturated) conditions.

In dry tests, the confining pressure was increased in steps of 5 MPa up to 50 MPa and in steps of 10 MPa from 50 to 100 MPa, with measurements of V_p conducted at each step. For V_p, the accuracy is estimated as 1–2%. A schematic diagram of the internal arrangement of the measurement apparatus is shown in Figure 5 [from *Heap et al.*, 2014a].

The apparatus is also equipped with two 70 MPa servo-controlled fluid pressure intensifiers that allow measurements in water-saturated samples at elevated pore fluid pressures. To prepare wet tests, the samples were saturated under vacuum with distilled water and then inserted in the pressure vessel. The confining pressure was set at 20 MPa and the pore fluid pressure at 4 MPa in both intensifiers, equivalent to an effective pressure (confining pressure minus pore pressure, for water-saturated tests) of 16 MPa and kept constant until pressure equilibrium was reached. Afterward, we imposed a pore fluid pressure difference (1 MPa) between the two intensifiers (P_up 4 MPa and P_down 3 MPa) and measured permeability at steps of effective pressure of 5 MPa. Permeability was measured generally for maximum effective pressure of 46 MPa, with the exceptions of samples (M1 and Ln11), for which effective pressures of 96 MPa were reached. Samples were kept at each confining pressure step until steady state flow conditions were achieved. We were then able to determine the permeability at each pressure step from the measured volume flow rates and the sample dimensions, using Darcy's law.

Two saturated samples were also tested under increasing confining pressure in order to calculate the porosity variation. For each increment in confining pressure, we measured the volume of expelled water and thus estimated the decrease in pore volume.

Table 1. Summary of the Physical Properties of the Different Lithologies Measured at Ambient Pressure (0 MPa) and at High Pressure (100 MPa)[a]

Group	Sample Name	Bulk Density (g/cm^3)	Porosity (%)	$Porosity_{AT}$ (%)	$V_{p0\ MPa}$ (m/s)	$V_{p100\ MPa}$ (m/s)	Permeability (m^2)	Stratigraphic Distance (m)
	Ln1	2.52	6.74		2429			80
	Ln2	2.63	2.63	1.12	4194	4774	1.362×10^{-15}	20
A1A1	Lp2	2.64	2.24	1.84	4192	4983		20
	Ln3	2.55	5.80	4.89	2544	4122		15
	Lp3	2.61	4.14		3907			15
	Ln4	2.58	4.49	3.55	2807	4648		270
	Lp4	2.57	4.75		2451			270
	Ln5	2.53	6.89		2441			140
A2A2	Lp5	2.51	7.47		2574			140
	Ln6	2.50	7.68		2374			280
	Ln7	2.63	2.99	2.94	3446	4729		210
	M1	2.58	5.15	4.71	2549	4685	2.197×10^{-15}	280
	Ln8	2.47	8.40	8.10	2067	3610		560
	Ln9	2.62	3.81	3.64	3202	4254		590
	Ln10	2.59	5.56	3.68	2408	4059		600
	Ln11	2.52	6.89	6.55	3144	4329	3.911×10^{-15}	735
	Lp11	2.52	6.12	5.61	3449	4572	2.640×10^{-15}	735
	Ln12	2.56	5.68	4.50	2331	4195		735
B	Ln13	2.52	7.26	6.79	2368	3824		735
	Ln14	2.58	5.23	5.10	3298	4174		735
	Ln15	2.31	13.83	12.05	1153	3285		840
	M2	2.61	4.00	1.25	1808	4387		735
	M3	2.57	5.42	4.86	2321	4674	3.020×10^{-15}	735
	M4	2.78	5.95	5.61	1960			690
	M5	2.57	5.53	4.80	1406	4122		735
	M6	2.53	7.12	6.79	927	3870		735

[a]Porosity is connected porosity, porosity AT is the porosity after tests at high pressure, and V_p is the *P* wave velocity. Stratigraphic distance is calculated from the thrust fault by measuring, perpendicularly to the bedding attitude, the distance between the sample location and the fault trace.

5. Results

5.1. Measurements at Ambient Pressure

Bulk densities, connected porosities, and axial *P* wave velocities measured at ambient pressure are listed in Table 1. Connected porosities and bulk densities range from 2.2% to 13.8% and from 2.3 g/cm^3 to 2.6 g/cm^3, respectively. At ambient pressure, parallel laminated samples (Lp) show that *P* wave velocities are higher than those of orthogonal samples (Ln) in both dry and saturated conditions (Figure 6a). Generally, laminated samples show a linear inverse relationship between porosity and axial *P* waves velocity (Figure 6a) in agreement with literature data [e.g., *Jaeger et al.*, 2007]. The measurements on massive sandstones show a comparable, although less constrained, correlation between the axial *P* wave velocity and porosity (Figure 6b), and for the same porosity value, they exhibit lower V_p with respect to laminated samples at ambient pressure.

5.2. Measurements at Elevated Pressure

In order to characterize the physical properties of the Frosinone Formation over the entire range of burial conditions, laboratory measurements were performed on six samples loaded up to 100 MPa confining pressure. These samples (Ln12, Ln13, Ln14, M2, M5, and M6) were cored at a stratigraphic distance of about 735 m from the Olevano–Antrodoco thrust fault and far from other secondary structures. *P* wave velocity measurements were conducted on dry samples during pressurization to 100 MPa and depressurization to ambient pressure both for laminated (Figure7a) and massive (Figure 7b) samples. With increasing pressure, the *P* wave velocity increases and values obtained during depressurization are always higher than those recorded during pressurization leading to a strong velocity hysteresis (Figures 7a and 7b).

It is possible to note a different trend between laminated and massive lithofacies. Laminated samples Ln12, Ln13, and Ln14 exhibit a total change of velocity of 80%, 62%, and 27%, respectively, with increasing pressure from 0 to 100 MPa, while the velocity variations were higher for the massive samples M2, M5, and M6

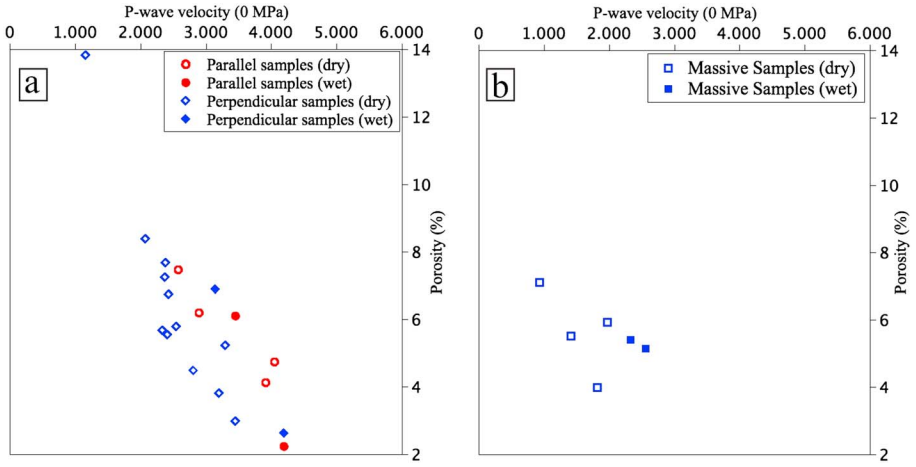

Figure 6. Variation of axial *P* wave velocity at ambient pressure as a function of porosity for (a) laminated and (b) massive samples.

(143%,193%, and 317%, respectively). For both laminated and (more evidently) massive samples, the velocity increase mostly occurred at low confining pressures, between 0 and 50 MPa. At confining pressures above 50 MPa, the low-porosity samples (M2 and Ln14) had relatively high *P* wave velocities, while the high-porosity ones (M6 and Ln13) were associated with lower velocities (Figures 7a and 7b).

5.3. Comparison Between Laboratory Data and Sonic Log Measurements

To test the reliability of our laboratory data for interpreting natural processes, we analyzed sonic logs of *P* wave velocities recorded from two boreholes (Frosinone 1 and Pilone 1), traversing the same stratigraphic unit (Frosinone Formation) some tens of kilometer southeast of the sampled area (see Figure 1 for well locations). We digitalized the sonic logs from the database of ViDEPI project (Ministero dello Sviluppo Economico, Italy; http://unmig.sviluppoeconomico.gov.it/videpi/) in order to infer digital velocity profiles from the interval transit times of sonic logs by using a sampling interval of 10 m.

The Frosinone 1 borehole penetrated the Frosinone Formation from about 170 to 510 m depth. The stratigraphic log indicates the presence of quartz-rich sandstones in alternance with levels of siltstones and claystones. The sonic log shows an average velocity of 3.4 km/s.

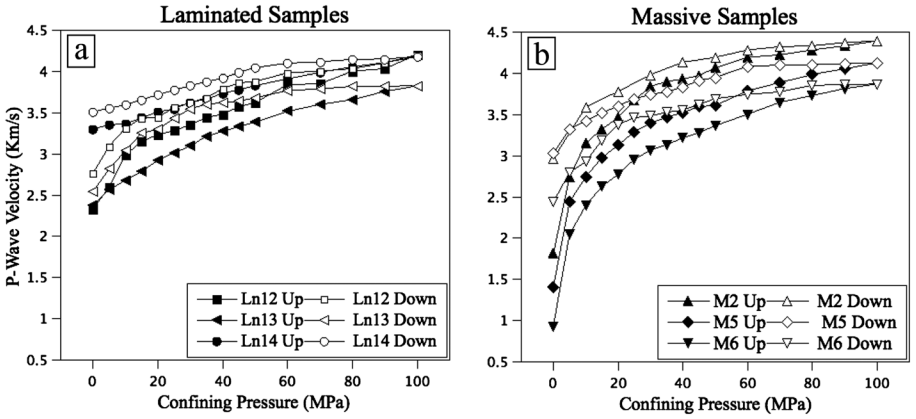

Figure 7. Variation of axial *P* wave velocity for representative samples of (a) laminated and (b) massive sandstones in dry conditions measured during both pressurization (solid symbols, up) and depressurization (open symbols, down) cycles. For all samples, the *P* wave velocities measured during depressurization are higher than those obtained during pressurization, suggesting that inelastic compaction is induced in the samples during pressurization up to 100 MPa.

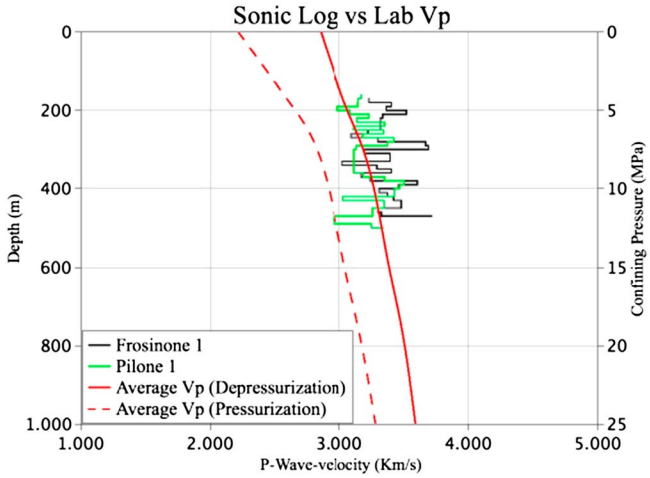

Figure 8. Comparison between synthetic V_p depth profile (calculated from the laboratory *P* wave velocities during pressurization and depressurization phases) and in situ V_p measurements from sonic logs through the Frosinone Formation at the Frosinone 1 and Pilone 1 boreholes. See Figure 1 for the borehole locations.

The Pilone 1 borehole penetrated the Frosinone Formation from about 160 to 550 m depth. The stratigraphic log shows the same lithological features observed for the Frosinone 1 borehole, and the sonic log is characterized by an average velocity of 3.2 km/s.

Synthetic profiles of seismic *P* wave velocity with increasing depth were calculated by using our average laboratory values from pressurization and depressurization cycles, assuming a mean lithostatic stress gradient of 25 MPa/km (Figure 8). Comparing laboratory and in situ velocities is difficult owing to differences in attenuation caused by different acquisition frequencies [*Batzle et al.*, 2006; *Chapman et al.*, 2006; *Adam et al.*, 2009; *Thakur and Rajput*, 2010, and references therein]. *Tisato and Madonna* [2012] showed that attenuation occurs if (1) fluids are present and (2) frequencies are higher than 10 Hz in rock samples hydrostatically confined at pressure lower than 2 MPa. Attenuation decreases progressively for confining pressures between 2 and 15 MPa. Above 15 MPa, no attenuation occurs irrespective of presence of fluids or frequency. Comparing laboratory and boreholes *P* wave velocity profiles, we used only oven-dried laboratory measurements (acquired at frequency = 1 MHz) to exclude attenuation problems. The depth steps of the borehole measurements (acquired at frequency = 10 Hz) corresponded to increments in confining pressure of >2 MPa and the maximum depth to about 13 MPa. Following *Tisato and Madonna* [2012] under these conditions, the discrepancy between laboratory data (dry samples) and in situ velocities (at 10 Hz and up to 13 MPa) should be reasonably low.

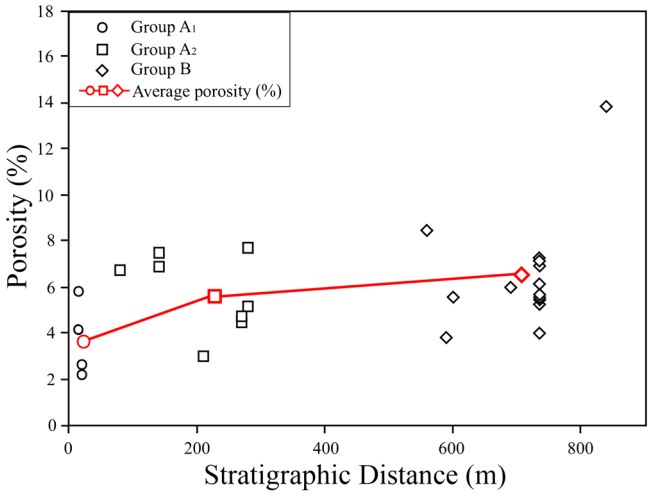

Figure 9. Variation of connected porosity as a function of the distance from the fault plane. Samples are divided into two groups: samples at a distance smaller than 300 m (group A) and samples at a distance larger than 300 m (group B). Group A was divided in two subgroups: samples in proximity of the fault, group A_1 (<50 m) and samples within the fault zone, group A_2 (>50 m and <300 m). The average effective porosity, calculated for each group, decreases toward the fault plane.

The comparison between synthetic and borehole profiles (Figure 8) demonstrate that borehole velocities are higher than laboratory values obtained during pressurization but closely match those velocities measured during depressurization. The lower velocities recorded at zero confining pressure at the onset of the test, respect to the in situ measurements extrapolated to the surface, is likely related to exhumation-related processes (e.g., long-term stress relief and associated crack reopening), while the velocity pressure sensitivity allow us to exclude weathering effects [*Morrow and Lockner*, 1994].

We conclude that (1) in situ measurements show a slight increase in velocity with increasing depth and (2) the in situ velocities are in the range of laboratory data recorded during depressurization cycle. This behavior confirms that compaction and

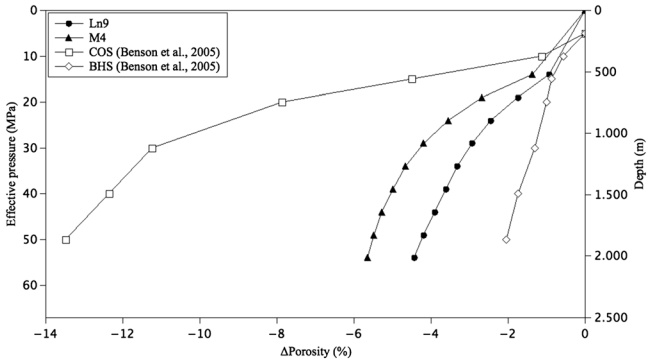

Figure 10. Relative changes in porosities as a function of effective pressure up to about 50 MPa, simulating up to 2 km of sedimentary burial [*Corrado*, 1994]. Porosity decreases by 4.4% and 5.7%, respectively, for Ln9 and M4 with increasing effective pressure. These values are in agreement with data for sandstones by *Benson et al.* [2005].

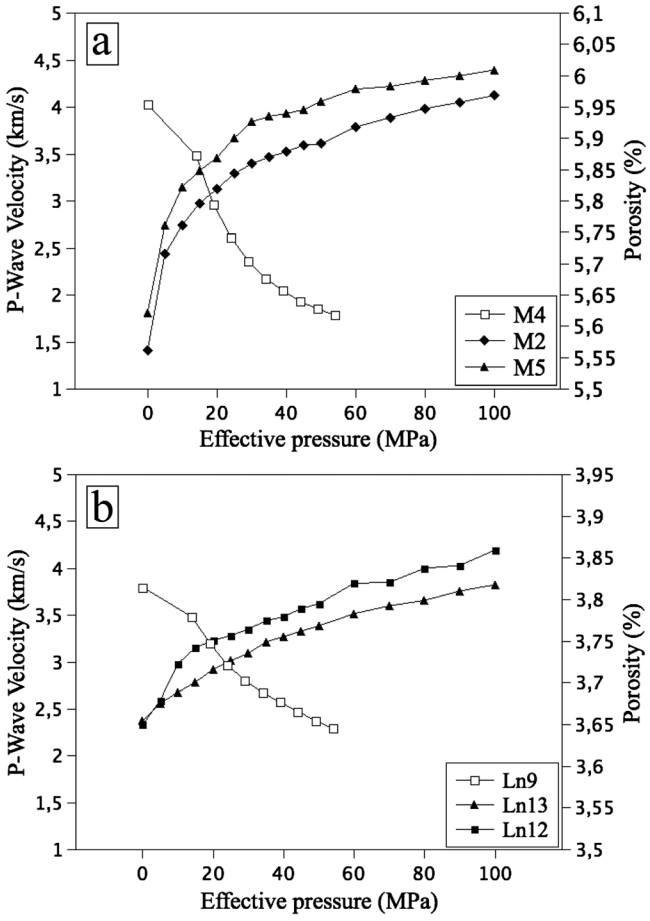

Figure 11. Variation of porositiy (open symbols) and axial *P* wave velocities measured under dry condition (solid symbols) during increasing effective pressure both for (a) massive and (b) laminated samples. Porosity decreases and axial *P* wave velocity increases for increasing pressure. The change in porosity mirrors the change in velocity. Porosities at ambient pressure of samples M4, M2, and M5 are, respectively, 5.9%, 4%, and 5.5%. Porosities of samples Ln9, Ln13, and Ln12 are, respectively, 3.8%, 7.3%, and 5.7%.

subsequent porosity decrease directly depend on the overburden pressure experienced by the rock volume in particular in the early stages of burial (first 2 km). This is in agreement with previous work [e.g., *Corrado*, 1994], indicating that all drilled rocks were previously buried at deeper depths and velocities hysteresis is recorded also in borehole sonic log.

5.4. Evolution of Sandstone Petrophysical Properties With the Distance From the Fault

With the aim of determining the evolution of petrophysical properties of sandstones with the stratigraphic distance from the fault plane, the whole data set was divided in two groups: group A comprised samples collected within the 300 m thick footwall damage zone, whereas group B comprised samples from larger distance. Group A was further divided in two subgroups accounting for samples taken in proximity of the fault plane, group A_1 (distance < 50 m), and samples from the damage zone, group A_2 ($50\ \text{m} <$ distance < 300 m) (Figure 9).

The porosity values are characterized by high variability as commonly observed for natural systems in both laboratory experiments [e.g., *Allen and Allen*, 2005] and from borehole data [e.g., *Bally et al.*, 1986; *Pierdominici et al.*, 2011]. In order to define a trend for the whole lithology, we calculated the average porosity of groups A_1, A_2, and B from porosity values of Table 1. Group A_1 shows an average porosity of 3.7% with a minimum value of 2.2% (sample Lp2), corresponding to the lowest value of the whole data set. Conversely, average porosities for group A_2 and B are, respectively, 5.8% and 6.5%. In spite of the great textural heterogeneity of Frosinone Formation, these variations highlight a relative porosity decrease of about 43% (from 6.5% to 3.7%) moving from the undeformed sandstones toward the sandstones close to the fault plane (Figure 9).

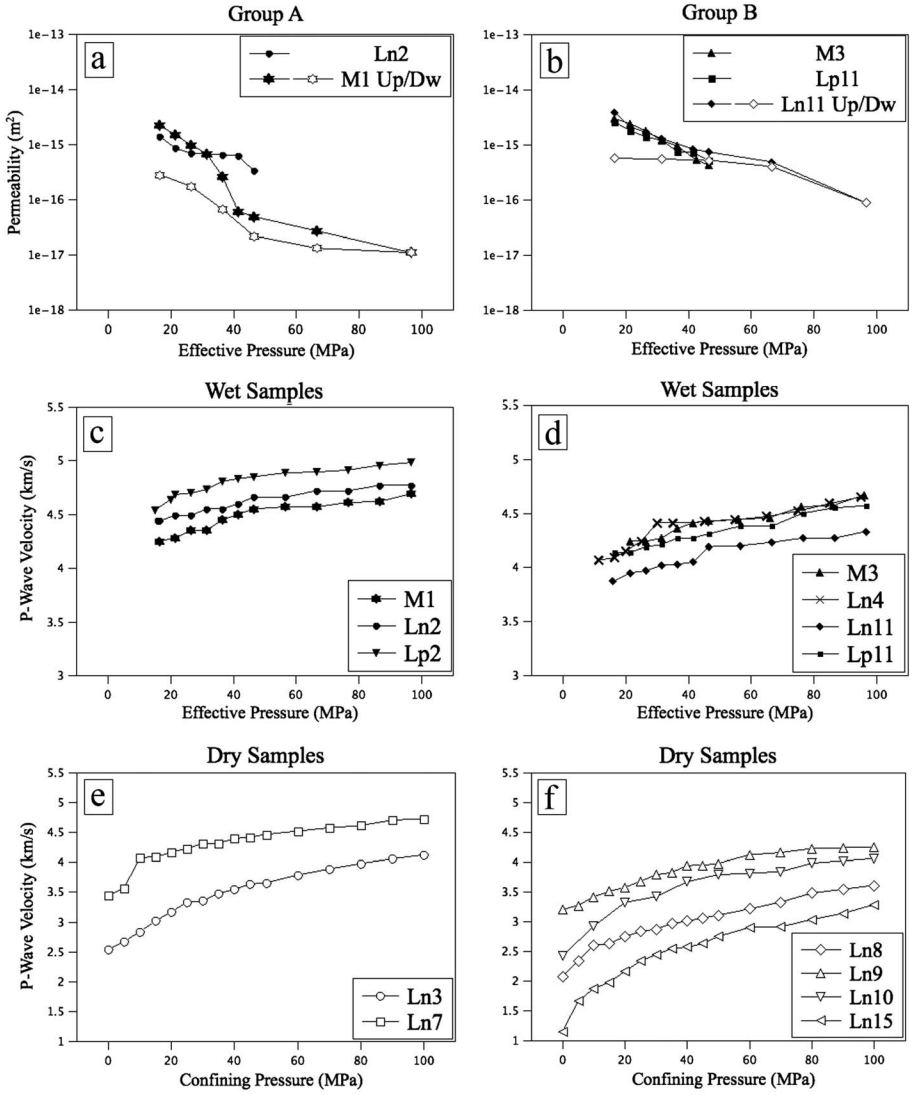

Figure 12. Variation of (a and b) permeabilities and (c and d) axial *P* wave velocities under both (e) wet and (f) dry conditions as a function of pressure and distance from the fault plane. Samples in proximity of the fault (group A) show lower permeabilities and higher *P* wave velocities than those sampled at larger distances (group B).

For two samples (M4 and Ln9), we also investigated the porosity change with increasing effective pressure. Porosity measurements were made at each increment in effective pressure, from 0 to 54 MPa, in order to simulate the maximum burial depth of 2 km [*Corrado*, 1994]. Results indicate that with increasing effective pressure, porosity decreases by 5.7% and 4.4%, respectively, for samples M4 and Ln9, in agreement with the porosity range reported by *Benson et al.* [2005] (Figure 10). These changes in porosities were negatively correlated with the evolution of *P* wave velocities both for massive (Figure 11a) and for laminated samples (Figure 11b). Due to the effect of microcracks closure, the largest porosity and *P* wave velocity changes are recorded in a pressure interval spanning between 0 and 50 MPa.

Figure 12 shows that the permeability measurements of group A (Figure 12a; samples Ln2 and M1) are generally lower than that of group B (Figure 12b; samples M3, Lp11, and Ln11), in agreement with porosity measurements. In particular, sample Ln2 shows the lowest initial permeability and porosity, respectively, of 1.4×10^{-15} m^2 and 2.6%; in contrast, sample Ln11 shows the highest initial permeability and porosity, respectively, of 3.9×10^{-15} m^2 and 6.9%.

Accordingly, *P* wave velocities of group A exhibit values higher than those measured for group B, both under saturated (Figures 12c and 12d) and dry conditions (Figures 12e and 12f). During depressurization cycle, the

permeability values and *P* wave velocities are invariably lower and faster than those measured during pressurization cycle. According to *Okazaki et al*. [2014], the porosities measured at ambient pressure after pressure tests are lower than those measured prior to the tests. This is in agreement with the hysteresis inferred from both velocity and permeability analyses (Table 1).

6. Discussion

Although all the analyzed samples pertain to the same rock formation, systematic petrophysical differences have been observed. These differences are mainly related to (1) the original depositional conditions that produced massive and laminated textures and (2) the distance from the Olevano–Antrodoco thrust fault.

As point (1) is concerned, our measurements conducted under ambient conditions show a linear inverse relationship between porosity and *P* wave velocity [e.g., *Chang et al*., 2006] for both laminated (Figure 6a) and massive (Figure 6b) samples; according to *Mavko et al*. [2009], sandstones have lower *P* wave velocity with increasing porosity and vice versa. This is consistent with the observation that the V_p behavior is essentially a measure of the bulk modulus of the rock (solid matrix, microcracks, and pores). Consequently, an increase of the number of microcracks corresponds to a decrease in *P* wave velocity [e.g., *Mavko et al*., 2009]. However, for comparable porosity, massive sandstones exhibit lower V_p with respect to laminated samples at ambient pressure. This is due to the distinct microstructural characteristics of sandstones. Examined under the optic microscope, massive samples show poorly sorted grains textures, lacking of internal organization, with large grains scattered in the matrix (Figures 4c and 4d). Massive samples are characterized by a larger number of microcracks compared to laminated samples. At ambient pressure, these microcracks were open and reduced significantly the *P* wave velocity with respect to laminated samples at the same conditions.

Seismic anisotropy in laminated samples is demonstrated by the fact that *P* waves velocities in Lp samples are faster than those measured in Ln samples. At ambient pressure, both water-saturated Lp and Ln samples show *P* wave velocities higher than those measured on dry samples. Similar results were obtained for high effective pressure, with saturated samples still exhibiting slightly higher *P* wave velocities. However, for these samples, the total change in *P* wave velocity with increasing effective pressure is much smaller (between 6% and 12%). At low effective pressures, microcracks were open and water-filled. Consequently, V_p was significantly higher in saturated rocks than in dry rocks. By contrast, at effective pressure higher than 50 MPa, the microcracks were essentially closed, implying a smaller difference in V_p as observed for other lithologies [*Trippetta et al*., 2010; *Heap et al*., 2009].

The discussed changes in seismic wave velocity are consistent with the variation of the lithological nature of the rock samples. For laminated samples, most of the velocity increase occurred at pressures below 50 MPa, with the rate of increase slowing markedly above this value.

At low pressures, seismic wave propagation is heavily influenced by cracks, since microcraks can still be open below 50 MPa [e.g., *Trippetta et al*., 2010]. For massive samples, we noted a larger and step-like change in velocity at pressure between 0 and 50 MPa with respect to laminated samples. From these results, it can be inferred that massive sandstones contain a significantly larger number of microcracks with respect to laminated samples as confirmed by microstructural observations (Figure 4).

The second factor controlling the petrophysical properties of the Frosinone Formation is the stratigraphic distance from the Olevano–Antrodoco thrust fault. It is worth noting that at the footwall of the Olevano–Antrodoco fault, the Frosinone Formation dips toward W-WSW and NW (Figure 2). Therefore, moving from E to W, younger strata progressively crop out. Due to the decrease in burial depth, permeability and porosity should increase, while *P* wave velocity should decrease. On the contrary, laboratory experiments revealed a decrease of porosity from 6.5% (group B) to 3.7% (group A_1) toward the Olevano–Antrodoco thrust fault (Figure 13). Moreover, the average permeability decreased, and average *P* wave velocity increased markedly from E to W (Figure 13). This can be interpreted as the effect of tectonic load caused by thrusting, where tectonic compaction overprinted the original sedimentary compaction, inverting the original permeability, porosity, and velocity trends.

At a more detailed scale, the structural control of the Olevano–Antrodoco thrust fault is suggested by the development of deformation bands [e.g., *Antonellini and Aydin*, 1994, 1995; *Eichhubl et al*., 2010; *Solum et al*., 2010]. Several studies demonstrated that close to a fault plane and within the damage zone, where

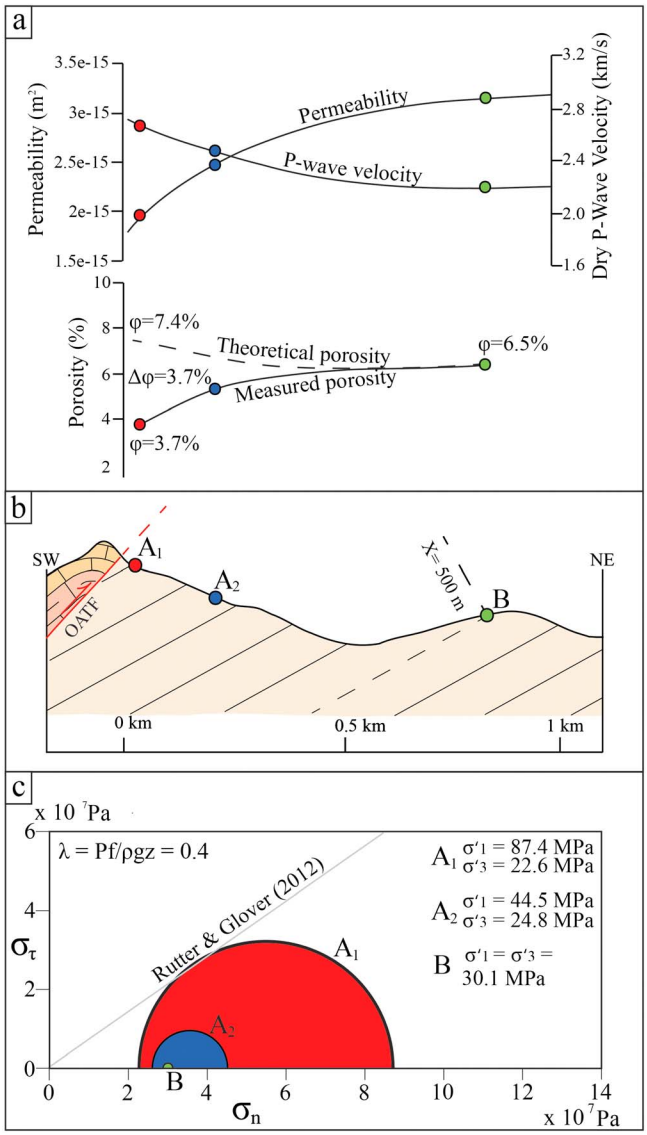

Figure 13. (a) Variation of petrophysical properties (average permeability and average dry *P* wave velocity at 0 MPa, average measured porosity, and theoretical porosity) as a function of the distance from the Olevano–Antrodoco thrust fault (OATF). (b) Structural and stratigraphic relationships between OATF and Frosinone Formation. (c) Mohr diagram showing the state of stress (effective stresses) close (point A_1) at about 200 m (point A_2) and at about 1 km away (point B) from the fault plane.

deformation bands are well developed, permeability and porosity are lower than in the undeformed rocks [e.g., *Zhu and Wong*, 1997; *Solum et al.*, 2010; *Wong and Baud*, 2012]. In our case, these observations are confirmed by sample Ln2, the only sample showing an incipient compaction band and characterized by among the lowest permeability and porosity values of the data set. In summary, our data showed a consistent kilometer-scale trend characterized by a decrease in porosity and permeability and an increase in *P* wave velocity approaching the fault plane (Figure 13a). These new data corroborate the observations from previous studies dealing with the behavior of sandstone-bearing faults [e.g., *Antonellini and Aydin*, 1994, 1995; *Solum et al.*, 2010; *Ballas et al.*, 2014].

6.1. Paleostress Reconstruction

In this section, we propose a new methodology to calculate differential paleostress needed to reach rupture conditions on exhumed faults using laboratory porosity measurements. The procedure is described graphically in Figures S1a–S1d in the supporting information.

The first step (Figure S1a in the supporting information) consists in assessing the porosity of sediments at the time of their deposition (initial porosity). The initial porosity is calculated for sediments cropping out ≈1 km away from the Olevano–Antrodoco thrust fault, since the sediments closer to the fault plane were likely affected both by sedimentary and tectonic loads. According to *Corrado* [1994], the maximum burial of footwall sediments of the Frosinone Formation at a distance of ≈1 km from the thrust fault (point B, Figure 13b) was about 2 km. Using this constraint, the initial porosity of the Frosinone Formation was calculated using the exponential porosity-depth relation [*Athy*, 1930]:

$$\phi = \phi_0 \exp^{-cx} \quad (1)$$

where ϕ is the porosity at depth x (km), ϕ_0 is the starting porosity of sediments, and c is an experimentally derived compaction coefficient. We assumed a compaction coefficient c equal to 0.27, typical for sandstones [*Sclater and Christie*, 1980]. From laboratory data, the average porosity of these sediments is $\phi = 6.5\%$ (Figure 9), for a burial depth of 2 km. Using equation (1), we calculated an initial (preburial) porosity $\phi_0 = 11.1\%$.

In the second step (Figure S1b in the supporting information), we calculated the maximum burial depth of point A_1 (close to the fault; Figure 13b) before the onset of faulting, in order to separate the effect of

sedimentary load from the subsequent tectonic load. From field data, the average dip angles of the Frosinone Formation and the fault plane are, respectively, about 30° and 47°. These geometric relationships suggested that point A_1 was, stratigraphically, 500 m shallower than point B (Figure 13b). As a consequence, the maximum burial depth of point A_1 was about 1500 m. Using equation (1), we calculated that the porosity of point A_1 related only to sedimentary load was about 7.4% (Figure 13a). It is worth noting that this value is higher than the porosity measured in laboratory for group A_1 (3.7%). The difference ($\Delta\phi = 3.7\%$, equal to inferred porosity minus calculated porosity) is thought to be caused by the tectonic load associated with the activity of the Olevano–Antrodoco thrust fault (Figure 13a).

In the third step (Figure S1c in the supporting information), we calculated the stress needed to reduce porosity of point A_1 from the theoretical value of 7.4% to the measured value of 3.7%. To this aim, we rearranged equation (1) as $x = \frac{\ln\left(\frac{\phi}{\Phi_0}\right)}{-c}$; by substituting x from the relation $\sigma = \rho g x$ and rearranging, we obtained

$$\sigma = \frac{\ln\left(\frac{\phi}{\phi_0}\right)}{-c}\rho\, g \tag{2}$$

where ϕ_0 is the porosity related only to sedimentary load (7.4%) and ϕ is the measured porosity (3.7%) (Figure 13a), ρ is the density (g/cm^3) of sediments, and g is the gravity acceleration. Assuming $\rho = 2.56$ g/cm^3 and $\sigma = 64.8$ MPa. This value represents the maximum differential stress ($\Delta\sigma$) that acted close to the fault plane (tectonic load) and reduced the porosity from 7.4% to 3.7% at a depth of 1500 m (point A_1; Figure 13a). Applying the same procedure to point A_2 and B, we obtained, respectively, $\Delta\sigma = 19.7$ MPa and $\Delta\sigma = 0$ MPa (no decrease in porosity due to tectonic loading).

In the final step (Figure S1d in the supporting information), we inferred the mechanical conditions of the system far (point B), at intermediate distance (point A_2) and close (point A_1) to the fault plane. First, we calculated $\sigma 3$ and $\sigma 1$. Our field data and previously published data [*Coli*, 1981; *Cavinato et al*., 1986; *Calamita and Deiana*, 1987; *Calamita et al*., 1987; *Corrado*, 1995; *Turtù et al*., 2013] indicated a compressional regime during the slip of the Olevano–Antrodoco thrust fault. This implies a horizontal $\sigma 1$ oriented SW-NE and a vertical $\sigma 3$. By using the density-depth relation, $\sigma = \rho g x$, it results that, $\sigma 3 = 37.7$ MPa as it corresponds to the vertical stress that acted at point A_1. Consequently, $\sigma 1$, calculated as $\sigma 1 = (\sigma 3 + \Delta\sigma) = (37.7\text{ MPa} + 64.8\text{ MPa})$, is about 102.5 MPa (Figure S1d in the supporting information). The same procedure was repeated for point A_2 (burial depth of 1650 m, $\Delta\sigma = 19.7$ MPa, $\sigma 1 = 61.1$ MPa, and $\sigma 3 = 41.4$ MPa) and for point B (burial depth of 2000 m, $\sigma 1 = \sigma 3 = 50.2$ MPa, since $\Delta\sigma = 0$) (Figure 13c).

In absence of evidence for fluid overpressure, a hydrostatic fluid pressure P_f ($\lambda = 0.4$, where $\lambda = P_f/\rho g x$) was assumed while reconstructing the paleostress state (Figure 13c); P_f resulted to be 15.1 MPa, 16.6 MPa, and 20.1 MPa for points A_1, A_2, and B, respectively. The effective stresses ($\sigma' = \sigma - P_f$) calculated for points A_1, A_2, and B are shown in Figure 13c.

Studies on friction by *Byerlee* [1978] considered numerous types of rocks and resulted into a range of coefficients of friction (μ) spanning from about 0.6 to 0.85. Following *Byerlee* [1978], accurate studies by *Rutter and Glover* [2012] suggested $\mu = 0.71$ for porous sandstones. We adopted this coefficient of friction in our paleostress reconstruction, assuming the Amontons criterion (cohesion $C = 0$), adequate for multiple episodes of reactivation of a fault. Under these conditions, failure was reached at point A_1; the Mohr circle is tangent to the failure envelope (Figure 13c), while stable conditions characterized points A_2 and B (Figure 13c). These results are fully consistent with geological observations and support the validity of the procedure. To check the stability of our calculations, a sensitivity analysis was performed on the paleostress reconstruction. We used the highest and the lowest porosities obtained for the samples of group A_1. This analysis showed that varying porosity throughout the entire range of measurements, the Mohr circles for point A_1 reach failure conditions within the range of friction proposed by *Byerlee* [1978] (see Figure S2a in the supporting information). Moreover, we tested the effect of fluid overpressures on the stability of our results. We found that if hydrostatic fluid pressure is increased by as much as 5 MPa, equivalent to $\lambda = 0.52$, the Mohr circles for point A_1 reach failure conditions within the range of friction proposed by *Byerlee* [1978] (Figure S2b in the supporting information). This denoted a good stability of our results and confirmed the reliability of the proposed procedure.

7. Conclusions

Laboratory measurements conducted on sandstones sampled at different distance from the Olevano–Antrodoco thrust fault and their comparison with analogue data from boreholes drilled in the same lithology allowed us to draw the following conclusions:

1. At ambient pressure, a linear inverse relationship was observed between porosity and *P* wave velocity in both laminated and massive samples.
2. With increasing confining pressure (from 0 to 100 MPa) under dry conditions, the average *P* wave velocity increased about 60% in laminated samples and about 200% in massive samples. The largest part of the velocity increase occurred in the pressure range between 0 and 50 MPa. At 0 MPa, the average *P* wave velocities for laminated and massive samples are about 2.5 km/s and 1.4 km/s, respectively. At 50 MPa and 100 MPa, the average *P* wave velocities are about 3.6 km/s and 4.1 km/s for both lithologies.
3. *P* wave velocities of boreholes logs matched well with the ultrasonic laboratory measurement measured during the depressurization cycle.
4. Permeability values ranged between $1.4\times10^{-15}\,m^2$ and $3.9\times10^{-15}\,m^2$ and were positively correlated with porosity values that spanned from 2.6% to 6.9%.
5. A constant decrease in porosity and permeability and an increase in *P* wave velocity are observed toward the Olevano–Antrodoco thrust fault. This allowed us to infer that the tectonic load increased the original sedimentary and diagenetic compaction of sediments, changing the petrophysical properties.

Finally, the mechanical reconstruction derived from inelastic compaction in the proximity of the fault plane indicated that the fault reached the mechanical condition for rupture in a compressive regime at a depth of 1500 m with a differential stress of 64.8 MPa.

Acknowledgments

Simone Fabbi and Salvatore Milli are thanked for their fruitful discussions. Domenico Mannetta is thanked for his help during the thin section preparation. We thank M.J. Heap and N. Tisato for the critical reviewing of this manuscript. Y. Bernabe is thanked for the constructive comments, which have been fundamental to improve the paper. Financial support from Progetti di Ateneo (Sapienza) 2012 (project "Fratturazione e stato termico in reservoir esposti, analoghi a quelli sepolti in Pianura Padana e Adriatico" led by Carminati Eugenio) is acknowledged. S. Mollo was supported by the ERC Starting Grant 259256 GLASS project. The research activities of the HP-HT laboratory of the INGV were supported by the European Observing System Infrastructure Project (EPOS). The data shown in Figures 6–136 to 13 can be requested from the corresponding author.

References

Accordi, G., F. Carbone, G. Civitelli, L. Corda, D. De Rita, D. Esu, and A. Sposato (1986), Lithofacies map of Latium-Abruzzi and neighbouring areas, scale 1:250000, Progetto Finalizzato Geodinamica, Consiglio Nazionale Riverche Italy, Roma.

Adam, L., M. Batzle, K. T. Lewallen, and K. Van Wijk (2009), Seismic wave attenuation in carbonates, *J. Geophys. Res.*, *114*, B06208, doi:10.1029/2008JB005890.

Agosta, F., M. Prasad, and A. Aydin (2007), Physical properties of carbonate fault rocks, fucino basin (Central Italy): Implications for fault seal in platform carbonates, *Geofluids*, *7*, 19–32.

Allen, P. A., and J. R. Allen (2005), *Basin Analysis, Principles and Applications*, 2nd ed., 549 pp., Blackwell Publishing, Oxford, U. K.

Antonellini, M., and A. Aydin (1994), Effect of faulting on fluid flow in porous sandstones: Petrophyisical properties, *AAPG Bull.*, *78*, 355–377.

Antonellini, M., and A. Aydin (1995), Effect of faulting on fluid flow in porous sandstones: Geometry and spatial distribution, *AAPG Bull.*, *79*, 642–670.

Athy, L. F. (1930), Density, porosity, and compaction of sedimentary rocks, *AAPG Bull.*, *14*, 1–24.

Aydin, A. (1978), Small faults formed as deformation bands in sandstones, *Pure Appl. Geophys.*, *116*, 913–930.

Ballas, G., R. Soliva, A. Benedicto, and J. P. Sizun (2014), Control of tectonic setting and large scale faults on the basin-scale distribution of deformation bands in porous sandstone (Provence, France), *Mar. Pet. Geol.*, *55*, 142–159, doi:10.1016/j.marpetgeo.2013.12.020.

Bally, A. W., L. Burbi, C. Cooper, and R. Ghelardoni (1986), Balanced sections and seismic reflection profiles across the Central Italy, *Mem. Soc. Geol. Ital.*, *35*, 257–310.

Barchi, M., A. De Feyter, B. Magnani, G. Minelli, G. Pialli, and B. Sotera (1998), The structural style of the Umbria-Marche fold and thrust belt, *Mem. Soc. Geol. Ital.*, *52*, 557–578.

Batzle, M. L., D.-H. Han, and R. Hofmann (2006), Fluid mobility and frequency-dependent seismic velocity — direct measurements, *Geophysics*, *71*(1), N1–N9, doi:10.1190/1.2159053.

Baud, P., W. Zhu, and T.-F. Wong (2000), Failure mode and weakening effect of water on sandstones, *J. Geophys. Res.*, *105*, 371–389, doi:10.1029/2000JB900087.

Baud, P., E. Klein, and T.-F. Wong (2004), Compaction localization in porous sandstones: Spatial evolution of damage and acoustic emission activity, *J. Struct. Geol.*, *26*, 603–624.

Benson, P. M., P. G. Meredith, E. S. Platzman, and R. E. White (2005), Pore fabric shape anisotropy in porous sandstones and its relation to elastic wave velocity and permeability anisotropy under hydrostatic pressure, *Int. J. Rock Mech. Min. Sci.*, *42*, 890–899.

Birch, F. (1960), The velocity of compressional waves in rocks to 10 kilobars, part 1, *J. Geophys. Res.*, *65*, 1083–1102, doi:10.1029/JZ065i004p01083.

Birch, F. (1961), The velocity of compressional waves in rocks to 10 kilobars, part 2, *J. Geophys. Res.*, *66*, 2199–2224, doi:10.1029/JZ066i007p02199.

Boccaletti, M., et al. (1990), Palinspastic restoration and paleogeographic reconstruction of the peri-Tyrrhenian area during the Neogene, *Paleogeogr. Paleoclimatol. Paleoecol.*, *77*, 41–50.

Butler, R. W. H., and S. Mazzoli (2006), Styles of continental contraction: A review and introduction, in *Styles of Continental Contraction*, *Geol. Soc. Am. Spec. Pap.*, vol. 414, edited by S. Mazzoli and R. W. H. Butler, pp. 1–10, Boulder, Colo.

Byerlee, J. D. (1978), Friction of rocks, *Pure Appl. Geophys.*, *116*, 615–626.

Caine, J. S., J. P. Evans, and C. B. Forster (1996), Fault zone architecture and permeability structure, *Geology*, *24*(11), 1025–1028.

Calamita, F. (1990), Thrust and fold-related structures in the Umbria-Marche Apennines (central Italy), *Ann. Tecton.*, *4*, 83–117.

Calamita, F., and G. Deiana (1987), The arcuate shape of the Umbia-Marche-Sabina Apennines (central Italy), *Tectonophysics*, *146*, 139–147.

Calamita, F., G. Deiana, C. Invernizzi, and S. Mastrovincenzo (1987), Analisi strutturale della "Linea Ancona-Anzio" Auct. Tra Cittareale e Micigliano (Rieti), *Boll. Soc. Geol. Ital.*, *106*, 365–375.

Cantelli, C., A. Castellarin, R. Colacicchi, and A. Praturlon (1982), La scarpata tettonica mesozoica lungo il settore nord della "Linea Ancona-Anzio", *Mem. Soc. Geol. Ital.*, *24*, 149–153.
Carminati, E., L. Corda, G. Mariotti, and M. Brandano (2007), Tectonic control on the architecture of a Miocene carbonate ramp in the Central Apennines (Italy): Insights from facies and backstripping analyses, *Sediment. Geol.*, *198*, 233–253.
Carminati, E., M. Lustrino, and C. Doglioni (2012), Geodynamic evolution of the central and western mediterranean: Tectonics vs. igneous petrology constraints, *Tectonophysics*, *579*, 173–192, doi:10.1016/j.tecto.2012.01.026.
Castellarin, A., R. Colacicchi, A. Praturlon, and C. Cantelli (1982), The Jurassic-lower Pliocene history of the Ancona-Anzio Line (central Italy), *Mem. Soc. Geol. Ital.*, *24*, 325–336.
Cavinato, G. P., and P. G. De Celles (1999), Extensional basins in the tectonically bimodal central Apennines fold-thrust belt, Italy: Response to corner flow above a subducting slab in retrograde motion, *Geology*, *27*, 955–958.
Cavinato, G. P., F. Salvini, and M. Tozzi (1986), Evoluzione strutturale del settore centrale della linea Olevano-Antrodoco, *Mem. Soc. Geol. Ital.*, *35*, 591–601.
Cello, G., and S. Mazzoli (1999), Apennine tectonics in Southern Italy: A review, *J. Geodyn.*, *27*, 191–211.
Cello, G., S. Mazzoli, E. Tondi, and E. Turco (1997), Active tectonics in the central Apennines and possible implications for seismic hazard analysis in peninsular Italy, *Tectonophysics*, *272*, 43–68.
Centamore, E., M. Chiocchini, G. Deiana, A. Micarelli, and U. Pieruccini (1971), Contributo alla conoscenza del Giurassico dell'Appennino Umbro-Marchigiano, *Stud. Geol. Camerti*, *1*, 1–89.
Chang, C., M. D. Zoback, and A. Khaksar (2006), Empirical relations between rock strength and physical properties in sedimentary rocks, *J. Pet. Sci. Eng.*, *51*, 223–237.
Chapman, M., E. Liu, and X.-Y. Li (2006), The influence of fluid-sensitive dispersion and attenuation on AVO analysis, *Geophys. J. Int.*, *167*, 89–105, doi:10.1111/j.1365-246X.2006.02919.x.
Chéry, J., M. D. Zoback, and S. Hickman (2004), A mechanical model of the San Andreas fault and SAFOD Pilot Hole stress measurements, *Geophys. Res. Lett.*, *31*, L15S13, doi:10.1029/2004GL019521.
Chester, F. M., and J. M. Logan (1986), Implication for mechanical properties of brittle faults from observations of the Punchbowl fault zone, California, *Pure Appl. Geophys.*, *124*, 79–106.
Cheung, C. S. N., P. Baud, and T.-F. Wong (2012), Effect of grain size distribution on the development of compaction localization in porous sandstone, *Geophys. Res. Lett.*, *39*, L21302, doi:10.1029/2012GL053739.
Chiocchini, U., N. Cipriani, G. Di Giacomo, D. Giacchetta, and F. Macri (1988), Petrografia delle arenarie torbiditiche tortoniane dei bacini laziali-abruzzesi, *Boll. Soc. Geol. Ital.*, *107*, 63–71.
Ciarapica, G., and L. Passeri (2005), Late Triassic and Early Jurassic sedimentary evolution of the Northern Apennines: An overview, *Boll. Soc. Geol. Ital.*, *124*, 189–201.
Ciccotti, M., and F. Mulargia (2004), Differences between static and dynamic elastic moduli of a typical seismogenic rock, *Geophys. J. Int.*, *157*, 474–477.
Ciccotti, M., R. Almagro, and F. Mulargia (2004), Static and dynamic moduli of the seismogenic layer in Italy, *Rock Mech. Rock Eng.*, *37*(3), 229–238.
Cipollari, P., and D. Cosentino (1991), La linea Olevano-Antrodoco: Contributo della biostratigrafia alla sua caratterizzazione cinematica, in *Studi Preliminari All'acquisizione Dati del Profilo CROP 11 Civitavecchia-Vasto*, *Stud. Geol. Camerti, Spec.*, vol. 1991/2, edited by M. Tozzi, G. P. Cavinato, and M. Parotto, pp. 143–149, Camerino, Italy.
Cipollari, P., D. Cosentino, and N. Perilli (1993), Analisi biostratigrafica dei depositi terrigeni a ridosso della linea Olevano-Antrodoco, *Geol. Rom.*, *29*, 495–513.
Cipollari, P., D. Cosentino, and M. Parotto (1995), *Modello Cinematico-Strutturale dell'Italia Centrale*, *Stud. Geol. Camerti, Spec.*, vol. 1995/2, pp. 135–143, Camerino, Italy.
Civitelli, G., and M. Brandano (2005), Atlante delle litofacies e modello deposizionale dei Calcari a Briozoi e Litotamni nella piattaforma carbonatica Laziale-Abruzzese, *Boll. Soc. Geol. Ital.*, *124*, 611–643.
Coli, M. (1981), Studio strutturale della "linea Ancona-Anzio" tra Posta ed Antrodoco (Gole del Velino), *Boll. Soc. Geol. Ital.*, *100*, 171–182.
Corrado, S. (1994), Analisi degli indicatori ottici di maturità della materia organica dispersa nei sedimenti: Un esempio di applicazione nell'Appennino centrale, *Boll. Soc. Geol. Ital.*, *113*, 645–673.
Corrado, S. (1995), Nuovi vincoli geometrico-cinematici all'evoluzione Neogenica del tratto meridionale della linea Olevano-Antrodoco, *Boll. Soc. Geol. Ital.*, *114*, 245–276.
Corrado, S., D. Di Bucci, G. Naso, and C. Faccenna (1998), Influence of paleogeography on thrust system geometries: An analogue modelling approach for the Abruzzi-Molise (Italy) case History, *Tectonophysics*, *296*, 437–453.
Cosentino, D., P. Cipollari, P. Marsili, and D. Scrocca (2010), Geology of the Central Apennines: A regional review, *J. Virtual Explor.*, *36*, paper 12, doi:10.3809/jvirtex.2010.00223.
Critelli, S., E. La Pera, F. Galluzzo, S. Milli, M. Moscatelli, S. Perrotta, and M. Santantonio (2007), Interpreting siliciclastic-carbonate detrital modes in foreland basin system: An example from Upper Miocene arenites of the central Apennines, Italy, *Geol. Soc. Am. Spec. Pap.*, *420*, 107–133.
Dallan Nardi, L., P. Elter, and R. Nardi (1971), Considerazioni sull'Arco dell'Appennino settentrionale e sulla "linea" Ancona-Anzio, *Boll. Soc. Geol. Ital.*, *90*, 203–211.
Damiani, A. V. (1990), Studi sulla piattaforma laziale-abruzzese. Nota II. Contributo all' interpretazione dell'evoluzione tettonico sedimentaria dei Monti Affilani e «pre-Ernici» e cenni sui rapporti con le adiacenti aree appenniniche, *Mem. Descr. Carta Geol. Ital.*, *38*, 177–206.
Damiani, A. V. (1991), *Riflessioni Sull'assetto Tettonico Della Dorsale Dei Monti Simbruini – Affilani – "Pre-Ernici" – Ernici e Nuove Ipotesi di Lavoro*, *Stud. Geol. Camerti, Spec.*, vol. 1991/2, pp. 63–66, Camerino, Italy.
Di Domenica, A., P. Petricca, F. Trippetta, E. Carminati, and F. Calamita (2014), Investigating fault reactivation during multiple tectonic inversions through mechanical and numerical modeling: An application to the Central-Northern Apennines of Italy, *J. Struct. Geol.*, *67*, 167–185, doi:10.1016/j.jsg.2014.07.018.
Eichhubl, P., J. N. Hooker, and S. E. Laubach (2010), Pure and shear-enhanced compaction bands in Aztec Sandstone, *J. Struct. Geol.*, *32*, 1873–1886, doi:10.1016/j.jsg.2010.02.004.
Faulkner, D. R., T. M. Mitchell, D. Healy, and M. J. Heap (2006), Slip on 'weak' faults by the rotation of regional stress in the fracture damage zone, *Nature*, *444*, 922–925, doi:10.1038/nature05353.
Fossen, H., R. A. Schultz, Z. K. Shipton, and K. Mair (2007), Deformation bands in sandstone: A rewiev, *J. Geol. Soc., London*, *164*, 1–15.
Glover, P. W. J., P. Baud, M. Darot, P. G. Meredith, S. A. Boon, M. Le Ravaleq, S. Zoussi, and T. Reusche (1995), α/β phase transition in quartz monitored using acoustic emissions, *Geophys. J. Int.*, *120*, 775–782, doi:10.1111/j.1365-246X.1995.tb01852.
Heap, M. J., S. Vinciguerra, and P. G. Meredith (2009), The evolution of elastic moduli with increasing crack damage during cyclic stressing of a basalt from Mt. Etna volcano, *Tectonophysics*, *471*, 153–160, doi:10.1016/j.tecto.2008.10.004.

Heap, M. J., P. Baud, P. G. Meredith, S. Vinciguerra, and T. Reuschlé (2014a), The permeability and elastic moduli of tuff from Campi Flegrei, Italy: Implications for ground deformation modelling, *Solid Earth*, *5*, 25–44.

Heap, M. J., Y. Lavallée, L. Petrakova, P. Baud, T. Reuschlé, N. R. Varley, and D. B. Dingwell (2014b), Microstructural controls on the physical and mechanical properties of edifice- forming andesites at Volcán de Colima, Mexico, *J. Geophys. Res. Solid Earth*, *119*, 2925–2963, doi:10.1002/2013JB010521.

Hickman, S., and M. Zoback (2004), Stress orientations and magnitudes in the SAFOD pilot hole, *Geophys. Res. Lett.*, *31*, L15S12, doi:10.1029/2004GL020043.

Jaeger, J., N. G. Cook, and R. Zimmerman (2007), *Foundamentals of Rock Mechanics*, 4th ed., 475 pp., Blackwell Publishing, Oxford, U. K.

Laubscher, H., and D. Bernoulli (1977), Mediterranean and Tethys, in *The Ocean Basins and Margins*, vol. 4, edited by A. E. M. Nairn, W. H. Kanes, and F. G. Stehli, pp. 1–28, Plenum Publ. Comp., New York.

Mavko, G., T. Mukerji, and J. Dvorkin (2009), *The Rock Physics Handbook: Tools for Seismic Analysis in Porous Media*, 2nd ed., 325 pp., Cambridge Univ. Press, Cambridge, U. K., and New York.

Milli, S., and S. Moscatelli (2000), Facies analysis and physical stratigraphy of the Messinian turbiditic complex in the Valle del Salto and Val di Varri (central Apennines), *G. Geol.*, *62*, 57–77.

Mitchell, T. M., and D. R. Faulkner (2012), Towards quantifying the matrix permeability of fault damage zones in low porosity rocks, *Earth Planet. Sci. Lett.*, *339–340*, 24–31, ISSN: 0012-821X, doi:10.1016/j.epsl.2012.05.014.

Montone, P., M. T. Mariucci, S. Pondrelli, and A. Amato (2012), An improved stress map for Italy and surrounding regions (central Mediterranean), *J. Geophys. Res.*, *109*, B10410, doi:10.1029/2003JB002703.

Morrow, C. A., and D. A. Lockner (1994), Permeability differences between surface-derived and deep drillhole core samples, *Geophys. Res. Lett.*, *21*, 2151–2154, doi:10.1029/94GL01936.

Mostardini, F., and S. Merlini (1986), Appennino centro-meridionale, sezioni geologiche e proposta di modello strutturale, *Mem. Soc. Geol. Ital.*, *35*, 177–202.

Okazaki, K., H. Noda, S. Uehara, and T. Shimamoto (2014), Permeability, porosity and pore geometry evolution during compaction of Neogene sedimentary rocks, *J. Struct. Geol.*, *62*, 1–12, doi:10.1016/j.jsg.2013.12.010.

Parotto, M., and A. Praturlon (1975), Geological summary of the Central Apennines, in *Structural Model of Italy*, *Quad. Ric. Scient.*, vol. 90, pp. 257–311, Natl. Res. Counc., Roma, Italy.

Patacca, E., and P. Scandone (1989), Post-Tortonian mountain building in the Apennines. The role of the passive sinking of a relic lithosphere slab, in *The Lithosphere in Italy, Advances in Earth Science Research*, edited by A. Boriani et al., pp. 157–176, Acc. Naz. Lincei, Roma.

Patacca, E., and P. Scandone (2001), Late thrust propagation and sedimentary response in the thrust belt-foredeep system of the Southern Apennines, in *Anatomy of an Orogen: The Apennines and Adjacent Mediterranean Basin*, edited by G. B. Vai and I. P. Martini, pp. 401–440, Kuwler Academic Publishers, Dordrecht, Netherlands.

Patacca, E., P. Scandone, M. Bellatalla, N. Perilli, and U. Santini (1991), *La Zona di Giunzione tra L'arco Appenninico Settentrionale e L'arco Appenninico Meridionale Nell'abruzzo e nel Molise*, *Stud. Geol. Camerti, Spec.*, vol. 1991/2, pp. 417–441, Camerino, Italy.

Pierantoni, P. P., G. Deiana, A. Romano, W. Paltrinieri, F. Borraccini, and S. Mazzoli (2005), Geometrie strutturali lungo la *thrust zone* del fronte montuoso umbro-marchigiano-sabino, *Boll. Soc. Geol. Ital.*, *124*, 395–411.

Pierdominici, S., M. T. Mariucci, and P. Montone (2011), A study to constrain the geometry of an active fault in southern Italy through borehole breakouts and downhole logs, *J. Geodyn.*, *52*(3–4), 279–289, ISSN: 0264-3707, doi:10.1016/j.jog.2011.02.006.

Ricci Lucchi, F. (1986), The Oligocene to recent foreland basins of the Northern Apennines, *IAS Spec. Publ.*, *8*, 105–139.

Royden, L., E. Patacca, and P. Scandone (1987), Segmentation and configuration of subducted lithosphere in Italy: An important control on thrust belt and foredeep basin evolution, *Geology*, *15*, 714–717.

Rutter, E. H., and C. T. Glover (2012), The deformation of porous sandstones; are Byerlee friction and the critical state line equivalent?, *J. Struct. Geol.*, *44*, 129–140.

Santantonio, M., and E. Carminati (2011), The Jurassic rifting evolution of the Apennines and Southern Alps (Italy): Parallels and differences, *Geol. Soc. Am. Bull.*, *123*, 468–484, doi:10.1130/b30104.1.

Sclater, J. G., and P. A. F. Christie (1980), Continental stretching: An explanation of the post-mid cretaceous subsidence of the central north basin, *J. Geophys. Res.*, *85*, 3711–3739, doi:10.1029/JB085iB07p03711.

Shipton, Z. K., and P. A. Cowie (2001), Damage zone and slip-surface evolution over μm to km scales in high-porosity Navajo sandstones, Utah, *J. Struct. Geol.*, *23*, 1825–1844.

Shipton, Z. K., J. P. Evans, K. R. Robeson, C. B. Forster, and S. Snelgrove (2002), Structural heterogeneity and permeability in faulted eolian sandstone: Implications for subsurface modeling of faults, *AAPG Bull.*, *86*, 863–883.

Solum, J. G., J. P. Brandenburg, S. J. Naruk, O. V. Kostenko, S. J. Wilkins, and R. A. Schultz (2010), Characterization of deformation bands associated with normal and reverse stress states in the Navajo Sandstone, Utah, *AAPG Bull.*, *94*, 1453–1475.

Tembe, S., D. Lockner, and T.-F. Wong (2009), Constraints on the stress state of the San Andreas Fault with analysis based on core and cuttings from San Andreas Fault Observatory at Depth (SAFOD) drilling phases 1 and 2, *J. Geophys. Res.*, *114*, B11401, doi:10.1029/2008JB005883.

Thakur, N., and S. Rajput (2010), *Exploration of Gas Hydrates*, 1st ed., 277 pp., Springer, Heidelberg, Germany.

Tisato, N., and C. Madonna (2012), Attenuation at low seismic frequencies in partially saturated rocks: Measurements and description of a new apparatus, *J. Appl. Geophys.*, *86*, 44–53.

Tondi, E., M. Antonellini, A. Aydin, L. Marchgiani, and G. Cello (2006), The role of deformation bands, stylolites and sheared stylolites in fault development in carbonate grainstones of Majella Mountain, Italy, *J. Struct. Geol.*, *28*, 376–391.

Trippetta, F., C. Collettini, S. Vinciguerra, and P. G. Meredith (2010), Laboratory measurements of the physical properties of Triassic Evaporites from Central Italy and correlation with geophysical data, *Tectonophysics*, *492*, 121–132, doi:10.1016/j.tecto.2010.06.001.

Trippetta, F., C. Collettini, P. G. Meredith, and S. Vinciguerra (2013), Evolution of the elastic moduli of seismogenic Triassic Evaporites subjected to cyclic stressing, *Tectonophysics*, *592*, 67–79, doi:10.1016/j.tecto.2013.02.011.

Turtù, A., S. Satolli, R. Maniscalco, F. Calamita, and F. Speranza (2013), Understanding progressive-arc- and strike-slip-related rotations in curve-shaped orogenic belts: The case of the Olevano-Antrodoco-Sibillini thrust (Northern Apennines, Italy), *J. Geophys. Res. Solid Earth*, *118*, 459–473, doi:10.1002/jgrb.50096.

Wong, T.-F., and P. Baud (2012), The brittle-ductile transition in porous rock: A review, *J. Struct. Geol.*, *44*, 25–53.

Wu, H.-Y., K. F. Ma, M. Zoback, N. Boness, H. Ito, J.-H. Hung, and S. Hickman (2007), Stress orientations of Taiwan Chelungpu-Fault Drilling Project (TCDP) hole-A as observed from geophysical logs, *Geophys. Res. Lett.*, *34*, L01303, doi:10.1029/2006GL028050.

Zhu, W., and T.-F. Wong (1997), The transition from brittle faulting to cataclastic flow: Permeability evolution, *J. Geophys. Res.*, *102*, 3027–3041, doi:10.1029/96JB03282.